

# Gas pathways and remotely triggered earthquakes beneath Mount Fuji, Japan

Koki Aizawa et al.

## **Analysis of the magnetotelluric (MT) data**

The MT method uses variations in the natural electromagnetic field to image subsurface resistivity structure. This procedure usually involves measuring two horizontal electrical field components ( $E_x$  and  $E_y$ ) and three magnetic field components ( $B_x$ ,  $B_y$ , and  $B_z$ ) of the electromagnetic field at the Earth's surface, where the subscripts  $x$ ,  $y$ , and  $z$  represent the N–S, E–W, and vertical components, respectively. The MT data were obtained in three campaigns. Between August and September 2009, audio-frequency band ( $\sim 0.0001$ – $1$  s) data were obtained to map the shallow structure ( $<3$  km) of the volcano. From June to December 2011, broad-band ( $\sim 0.0003$ – $820$  s) MT data were obtained to elucidate the deep structure where the triggered earthquakes originated, with a follow-up campaign from April to May 2012. In addition to these data, we used broad-band MT data collected in 2002–2003 along an ENE–WSW trending line across the volcano (Aizawa et al., 2004). From these data,

The resistivity structure is deduced in two steps: 1) an initial estimation of the MT response functions; and 2) inversions to determine the best fit to the observed MT response functions. For the 2009 AMT survey, the MT response functions were calculated using the SSMT2000 program, developed at Phoenix Geophysics. We also employed remote-reference processing (Gamble et al., 1979) for 0.2–1.3 s periods, using MT data recorded at the Esashi Magnetic Observatory, which is located 500 km NNE of Mt. Fuji. Note that the vertical magnetic field was not recorded in 2009 to reduce the effort of the field campaign. The MT response functions were calculated using a robust estimation code (Chave and Thomson, 2004) for the data collected during the 2011–2012 surveys. We also employed remote-reference processing (Gamble et al., 1979) for periods  $<10$  s, using MT data recorded at other the MT sites. The 1-Hz-sampled geomagnetic data recorded at the Kakioka Magnetic Observatory

(located 160 km NE of Mt. Fuji) were used for remote-reference processing of the MT data with periods  $>10$  s. Using this approach, we obtained the MT response functions across a broad period range of 0.0001–820 s. The periods of the MT response functions in 2002–2003 and 2009 differ slightly from the MT data in 2011–2012 due to the differences in sampling frequencies. We interpolated the MT response functions and error bars before 2011 in the frequency domain by using a cubic spline function. The MT response functions were then defined at the frequencies for 2011–2012.

The 2011–2012 MT data were obtained after the 2011 Tohoku–Oki and the Mw 5.9 earthquakes, thus necessitating an evaluation of the temporal change in resistivity structure between 2002 and 2012. Since some measurement sites in 2011–2012 overlap with the sites from either 2002–2003 or 2009, any changes in the MT response functions can be investigated. Figure S1 provides a comparison of the sounding curves; no significant change in the data is observed for periods  $<1$  s., and we assume that the resistivity structure did not change significantly from the earthquake sequence.

A 3-D inversion of the Mt. Fuji region was conducted with WSINV3DMT (Siripunvaraporn and Egbert, 2009). We used the full impedance tensor (four complex components:  $Z_{xx}$ ,  $Z_{xy}$ ,  $Z_{yx}$ , and  $Z_{yy}$ ) as the inputs for the 3-D inversion. While the 3-D inversion is inherently free from the 2-D limitations, we need to omit some MT sites in the inversion due to the trade-off between spatial resolution and computation time. A minimum 3-D horizontal mesh size of 800 m was set around the observation sites, which is coarser than the minimum 2-D horizontal mesh size of 500 m around the focal region of the Mw 5.9 earthquake. The 3-D horizontal mesh size was logarithmically increased with increasing distance from the summit of Mt. Fuji for locations away from the observation sites. The 3-D model also accounts for topography, with a vertical mesh size set at 200 m from the highest point to sea level, with the air approximated by  $10^8 \Omega\text{-m}$  blocks. A vertical mesh size of 300–1000 m was set from sea level to 21 km b.s.l., with a further increased mesh size employed below 21 km b.s.l. depth. The total mesh consisted of  $66 \times 66 \times 57$  units (with seven vertical air layers as the default setting) in the x, y, and z directions, respectively. Since the co-ordinate system was rotated  $30^\circ$  clockwise, the x and y directions correspond to N30°E and N120°E, respectively. The calculation area was  $322 \times 322 \times 265$  km, in which the ocean and bathymetry were represented by  $0.25 \Omega\text{-m}$  blocks (Fig. S2). The initial resistivity of

the land was set to 100  $\Omega$ -m. We omitted the diagonal components of the impedance tensor at periods  $<1$  s. In each iteration, we replaced the prior model by the smallest-misfit model of the previous iteration. We assumed constant 10% uncertainties for the impedance tensor. By using a smoothing parameter ( $\tau = 10$  with  $\delta x = \delta y = \delta z = 0.1$ ) in the model covariance matrix (Siripunvaraporn and Egbert, 2007), the normalised RMS misfit was reduced to 2.42 after six iterations. Figure S3 represents an example of the data fit shown by comparing sounding curves. The features in the apparent resistivity and phase curves around the focal region are well reproduced.

To validate the presence of the approximately N20°E–S20°W trending elongate conductive zones in the 3-D model, sensitivity tests were performed. First, resistivities  $<3000$   $\Omega$ -m around the focal region of the Mw 5.9 earthquake (model space spanning  $-11,000$  m  $< x < 800$  m,  $-8000$  m  $< y < 8000$  m, and  $-16,000$  m  $< z < -2200$  m) were all changed to 3000  $\Omega$ -m (Fig. S4). This elimination of the sub-vertical conductive zone resulted in an increase of the RMS misfit from 2.42 to 2.69; the corresponding changes in the sounding curves are presented in Figure S8. The same sensitivity test was also applied to the northern conductive zone (model space spanning  $-800$  m  $< x < 11,000$  m,  $-8000 < y < 8000$ , and  $-16,000$  m  $< z < -2200$  m). This elimination of the northern conductive zone resulted in an increase of the RMS misfit from 2.42 to 2.93; the corresponding changes in the sounding curves are shown in Figure S5. The sensitivity tests validated that the northern and southern sub-vertical conductive zones are necessary to explain the MT observations.

### Isotope analysis

Groundwater sampling for  $^3\text{He}/^4\text{He}$ ,  $\delta\text{D}$  and  $\delta^{18}\text{O}$  isotope analysis was conducted on February and March 2010, with the exception of site JRK (sampling in February 2012). The sampling points and site names are shown in Figure S6. Water samples were collected in 50 cm<sup>3</sup> glass containers fitted with high-vacuum stopcocks at both ends. A groundwater sample was pumped and channelled into the container using a double-mouth syringe connected to the other end of the container.

Magmatic helium, which is enriched in  $^3\text{He}$  relative to atmospheric helium, is continuously diluted with radiogenic  $^4\text{He}$  acquired from the U- and Th-rich crust; therefore, high  $^3\text{He}/^4\text{He}$  ratios indicates the contribution of magmatic helium

Dissolved gases in the water samples were extracted and analysed for helium isotope ratios, along with  $^4\text{He}$  and  $^{20}\text{Ne}$  concentrations, at the Geochemical Research Center at the University of Tokyo. The gas extraction was conducted using an all-metal Toepler pump, which quantitatively collects gas extracted from the water by ultrasonic vibration, with a yield of >99.9 vol.% (Padron et al., 2013). The remaining water after the gas extraction was used for  $\delta\text{D}$  and  $\delta^{18}\text{O}$  analyses. The collected gas was directly transferred into a noble gas purification line of a mass spectrometry system. Two mass spectrometer systems were used in this study: an MS-III equipped with a single collector system, and an MS-IV with a split-type flight tube and double collector system used for helium isotopes. Details of the experimental procedures for noble gas purification and measurements, using both the MS-III and MS-IV systems respectively, have been described in detail in earlier studies (Sumino et al., 2001; Kotarba and Napo, 2008). Air standards were measured frequently during the analyses to determine the mass spectrometer sensitivities. Calibration of the  $^3\text{He}/^4\text{He}$  ratios was performed using an inter-laboratory helium standard named HESJ, with a recommended  $^3\text{He}/^4\text{He}$  ratio of  $20.63 \pm 0.10 R_A$  (Matsuda et al., 2002). 1-sigma uncertainties are reported for the  $^3\text{He}/^4\text{He}$  ratios, which include errors from the measured raw  $^3\text{He}/^4\text{He}$  ratios, the measured raw  $^3\text{He}/^4\text{He}$  ratio of HESJ, and the recommended  $^3\text{He}/^4\text{He}$  ratio of HESJ. Concentration errors are estimated to be 5%, based on the reproducibility of noble gas sensitivity of the mass spectrometer during repeated air standard analyses. Procedural blank levels were  $1\text{--}2 \times 10^{-10}$  and  $3\text{--}5 \times 10^{-10} \text{ cm}^3 \text{ STP}$  for  $^4\text{He}$  and  $^{20}\text{Ne}$ , respectively, with an atmospheric  $^3\text{He}/^4\text{He}$  ratio. The blank levels are several orders of magnitude lower than the amounts of the sample gases, making any blank correction unnecessary.  $^3\text{He}/^4\text{He}$  ratios are corrected for atmospheric contamination by using  $^4\text{He}/^{20}\text{Ne}$  ratios of the samples and the value at 10 °C ASW (0.256, (Ozima and Podosek, 2002)). The results are presented in Table DR1.

Hydrogen and oxygen isotope ratios were measured by isotope-ratio mass spectrometry with dual inlet system (DELTA V Advantage and DELTA Plus, Thermo Fisher Scientific Inc., respectively). Sample waters for hydrogen and oxygen isotope analyses were reduced to  $\text{H}_2$  using 800 °C Cr metal (H-device, Thermo Fisher Scientific Inc.) and equilibrated with  $\text{CO}_2$  (Equilibrium system, Thermo Fisher Scientific Inc.) at the Geological Survey of Japan. Carbon isotope ratio was measured by continuous flow

isotope-ratio mass spectrometry (CF-IRMS) with a gas chromatography system (DELTA V Advantage and Gas Bench II, Thermo Fisher Scientific Inc.) at the Geological Survey of Japan. CO<sub>2</sub> samples were extracted using the headspace method with the addition of phosphoric acid. The total concentration of dissolved inorganic carbon was determined using peak area of CF-IRMS. The  $\delta$ -notations of isotopic values are conventionally represented with respect to the V-SMOW for  $\delta$ D and  $\delta^{18}\text{O}$  and V-PDB for  $\delta^{13}\text{C}$ . The measurement errors of  $\delta$ D,  $\delta^{18}\text{O}$  and  $\delta^{13}\text{C}$  are better than to be  $\pm 1\text{‰}$ ,  $\pm 0.1\text{‰}$  and  $\pm 0.1\text{‰}$ , respectively. Anion and cation concentrations were determined by ion chromatography (Thermo Fisher Scientific Inc. ICS-2100). The results are presented in Table DR2.

Regarding magmatic H<sub>2</sub>O, a possible small shift from meteoric values is within the scatter of the original data used to draw the meteoric line in Fig. 2c in Yasuhara et al. (2007), [www.mfri.pref.yamanashi.jp/fujikazan/original/P389-405.pdf](http://www.mfri.pref.yamanashi.jp/fujikazan/original/P389-405.pdf)). Therefore, we conclude that no evidence has been found to show the presence of magmatic water at a depth of 1000–2000 m. The contribution of magmatic H<sub>2</sub>O is, if any, considered to be not significant.

Possible magmatic H<sub>2</sub>O concentrations were calculated using the CO<sub>2</sub>/<sup>3</sup>He ratio and H<sub>2</sub>O/CO<sub>2</sub> ratio in previous works. Using the CO<sub>2</sub>/<sup>3</sup>He ratio of  $15.7 \times 10^9$  (mol/mol) from Sano and Williams (1996, GRL), which includes values from nearby Hakone volcano, we calculated the magmatic CO<sub>2</sub> value as 21.1–6020 mg/L (magmatic C: 5.8–1640 mg/L) at the depth of the sampling points. Magmatic H<sub>2</sub>O concentrations were calculated using the global island-arc type H<sub>2</sub>O/CO<sub>2</sub> ratio of 19 (mol/mol), which was obtained from high-temperature volcanic gas data (table 2 in Fischer, 2008). The results show that 0.03–4.62 wt% magmatic water is expected at the sampling depths. Using the H<sub>2</sub>O/CO<sub>2</sub> ratio of 4 (mol/mol) from the primary CO<sub>2</sub> contents of arc basaltic magmas (Wallace, 2005), a 0.01–0.97 wt% magmatic water fraction is expected. These small values seem consistent with observations that the presence of magmatic water is not significant at depths of 1000–2000 m. The absence of magmatic water is also suggested by the small Li/Cl ratios in groundwater (as low as 0.001; Table S2 and (Kazahaya et al., 2014)).

### **Calculation of advective overpressure**

In the ideal advective overpressure model such as that presented in the original research paper (Sahagian and Proussevitch, 1992), pore pressure rise is written as  $\rho g \Delta h$ , where  $\rho$  is the density,  $g$  the gravitational acceleration, and  $\Delta h$  the vertical travel of the bubble. However, in real circumstances, compressibility of the "container" and "fluid" reduces the effect of advective overpressure. The effect of advective overpressure also decreases as an amount of bubbles decreases. In the calculation of advective overpressure (Fig. 4), we applied equation (15) of Gross and Peters (2013), and assumed the bulk modulus of water (2.3 GPa), the bulk modulus of the surrounding rocks (10 GPa), and the confining pressure at a depth of 10 km depth (250 MPa). In equation (15), we neglected the effect of dead volume. Note that we do not model the pore pressure change of single crack, but model the entire pressure change of fractured zone (gas pathway, which was found by the observations).

In a simple case (Sahagian and Proussevitch, 1992), the pressure in a bubble at any time is the same as the pressure of surrounding liquid; therefore, resorption of bubbles cannot occur. The effect of resorption is also negligible even when fluid compressibility is taken into account, as the pressure in the rising bubble does not increase but rather decreases in the case of compressible fluids. However, resorption can occur in cases where some bubbles rise while others do not. Resorption reduce the effect of advective overpressure. However, in this study, we did not consider such a complex case, as it requires that the solubility, temperature, and composition of the gases, as well as the percentage of bubbles rising by seismic shaking, to be known. Alternatively, we assumed the simple case that (1) groundwater is initially saturated with gas in bubbles, and (2) all bubbles start to rise at the same rate in a fracture mesh of compressible ground water and compressible rock,

### **References in Supplementary material**

- Chave, A.D., and Thomson, D.J., 2004, Bounded influence magnetotelluric response function estimation: *Geophysical Journal International*, v. 157, p. 988-1006.
- Gamble, T.D., Clarke, J., and Goubau, W.M., 1979, *Magnetotellurics with a remote*

- magnetic reference: *Geophysics*, v. 44, p. 53-68.
- Gross, T.F., and Peters, F., 2013, The pressure in an enclosed volume of liquid in case of a rising bubble: *Acta Mechanica*, v. 224, p. 1685-1694.
- Kazahaya, K., Takahashi, M., Yasuhara, M., Nishio, Y., Inamura, A., Morikawa, N., Sato, T., Takahashi, H.A., Kitaoka, K., Ohsawa, S., Oyama, Y., Ohwada, M., Tsukamoto, H., Horiguchi, K., Tosaki, Y., and Kirita, T., 2014, Spatial distribution and feature of slab-related deep-seated fluid in SW Japan: *Journal of Japanese Association of Hydrological Sciences*, v. 44, p. 3-16.
- Kotarba, M.J., and Napo, K., 2008, Composition and origin of natural gases accumulated in the Polish and Ukrainian parts of the Carpathian region: Gaseous hydrocarbons, noble gases, carbon dioxide and nitrogen: *Chemical Geology*, v. 255, p. 426-438.
- Matsuda, J., Matsumoto, T., Sumino, H., Nagao, K., Yammaoto, J., Miura, Y., Kaneoka, I., Takahata, N., and Sano, Y., 2002, The He-3/He-4 ratio of the new internal He Standard of Japan (HESJ): *Geochemical Journal*, v. 36, p. 191-195.
- Ozima, M., and Podosek, F., 2002, *A. Noble Gas Geochemistry* 2nd edn. (Cambridge University Press), p. 389-405.
- Padron, E., Perez, N.M., Hernandez, P.A., Sumino, H., Melian, G.V., Barrancos, J., Nolasco, D., Padilla, G., Dionis, S., Rodriguez, F., Hernandez, I., Calvo, D., Peraza, M.D., and Nagao, K., 2013, Diffusive helium emissions as a precursory sign of volcanic unrest: *Geology*, v. 41, p. 539-542.
- Siripunvaraporn, W., and Egbert, G., 2007, Data space conjugate gradient inversion for 2-D magnetotelluric data: *Geophysical Journal International*, v. 170, p. 986-994.
- , 2009, WSINV3DMT: Vertical magnetic field transfer function inversion and parallel implementation: *Physics of the Earth and Planetary Interiors*, v. 173, p. 317-329.
- Sumino, H., Nagao, K., and Notsu, K., 2001, Highly sensitive and precise measurement of helium isotopes using a mass spectrometer with double collector system: *Journal of the Mass Spectrometry Society of Japan*, v. 49, p. 61-68.
- Yasuhara, M., Kazahaya, K., and Marui, A., 2007, An isotopic study on where, when and how groundwater is recharged in Fuji volcano, Central Japan: "Fuji volcano", eds. by S. Aramaki, T. Fujii, S. Nakada, and N. Miyaji, p. 389-405.

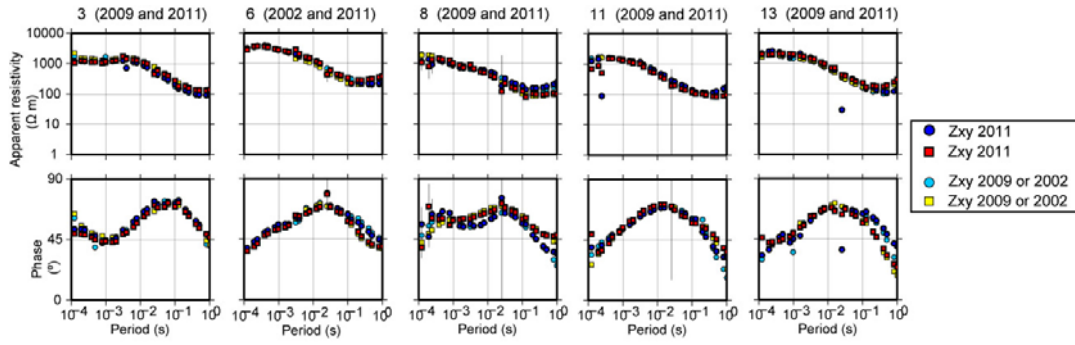


**Figure DR1.** Sounding curve comparisons between the MT data collected during the 2002–2003, 2009, and 2011–2012 surveys. Data before and after the 2011 Tohoku–Oki and Mw 5.9 earthquakes are compared. The x and y subscripts represent the north and east directions, respectively.  $180^\circ$  is added to the phase of  $Z_{yx}$  to enable comparisons between  $Z_{xy}$  and  $Z_{yx}$ . The MT site name, along with the survey data presented, is given above each panel; the MT sites presented are also identified in Figure S2. The off-diagonal components of the impedance tensor are shown for simplicity.

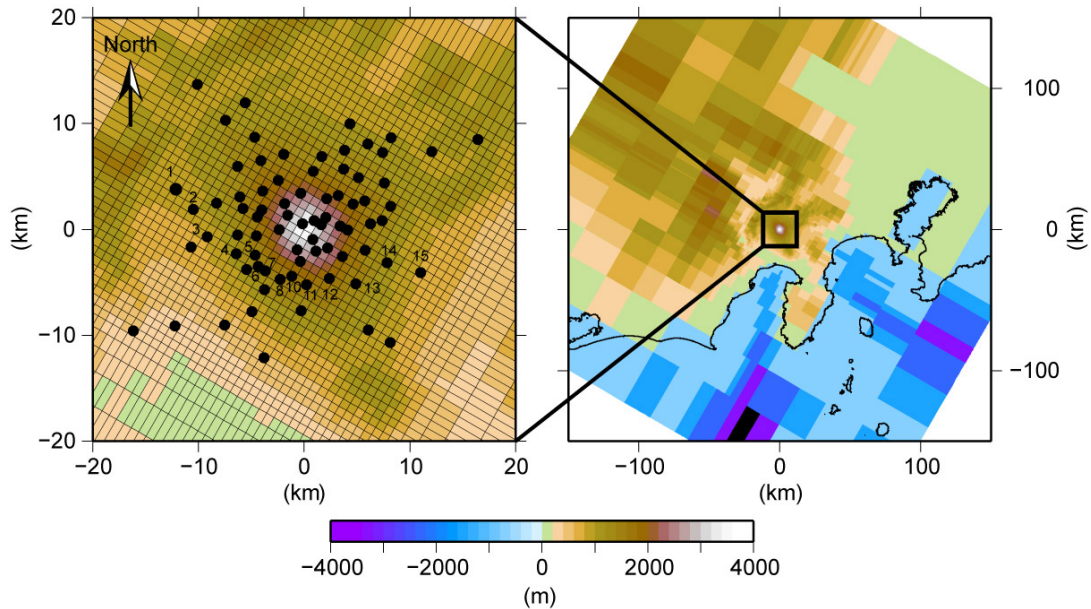


**Figure DR2.** Mesh used in the 3-D inversion. The solid circles show the MT measurement sites used in the inversion.



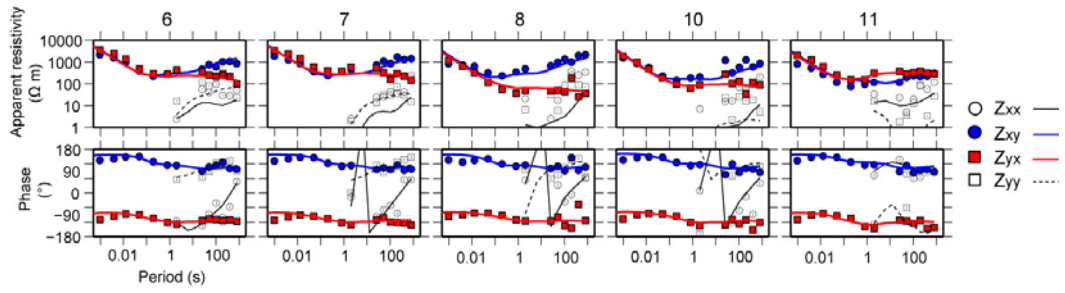


**Figure DR3.** Sounding curve comparisons between the observed MT data (symbols) and the calculated MT response (lines). MT sites around the focal region of the Mw 5.9 earthquake are shown (site names are shown in Fig. S2). Site 9 was omitted in the inversion due to the trade-off between spatial resolution and computation time. The calculated error bars are smaller than each symbol. Note that the parts of the diagonal components ( $Z_{xx}$  and  $Z_{yy}$ ) with periods of  $<1$  s were not used in the inversion.

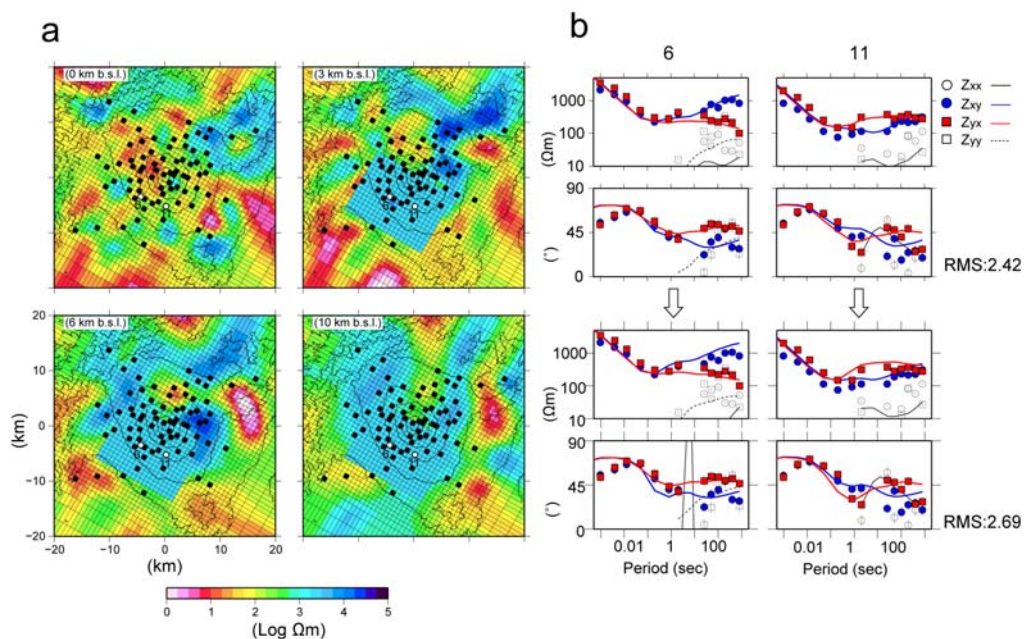


**Figure DR4.** Sensitivity test results. **(a)** Modified resistivity structure with no sub-vertical conductive zone that is coincident with the Mw 5.9 earthquake location. **(b)** Sounding curves calculated from the final (upper panel; Fig. 3) and modified (lower panel) resistivity structures. MT sites 6 and 11 are shown as open circles in (a).

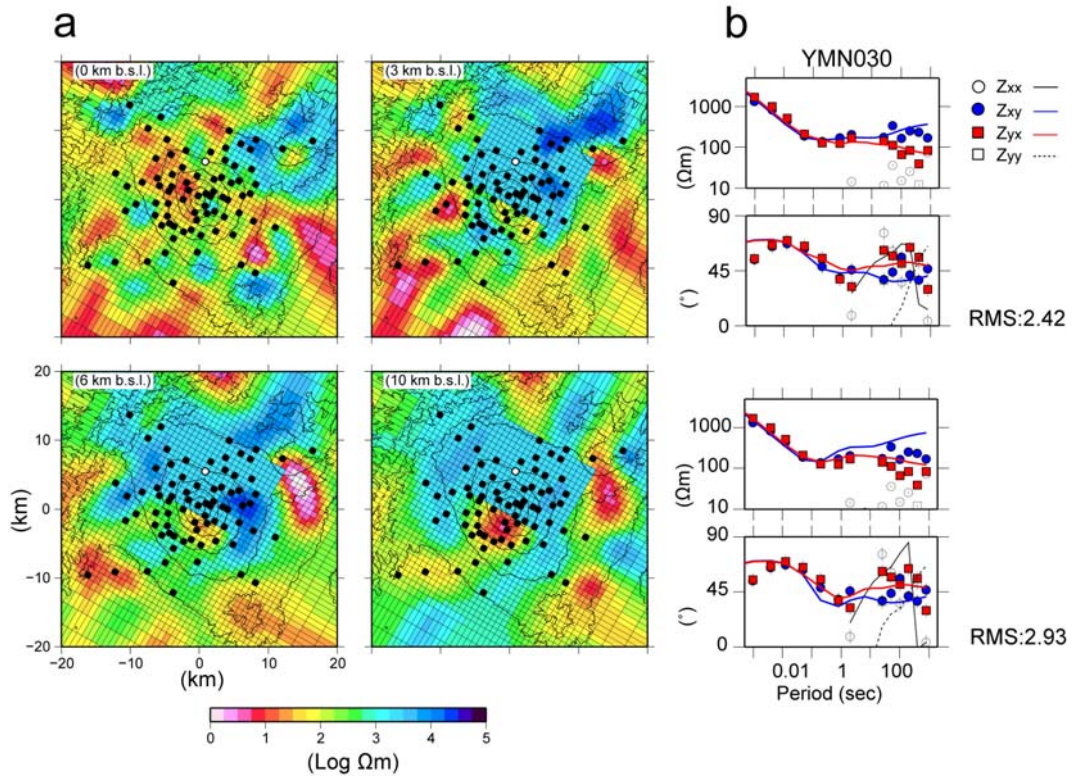


**Figure DR5.** Sensitivity test results from the resistivity inversion. **(a)** Modified resistivity structure with no conductive zone present beneath the northern region of Mt. Fuji. **(b)** A comparison of the calculated sounding curves from the final (upper) and modified (lower) resistivity structures. MT site YMN030 is shown as an open circle in (a). All notations are the same as in Figure S4.

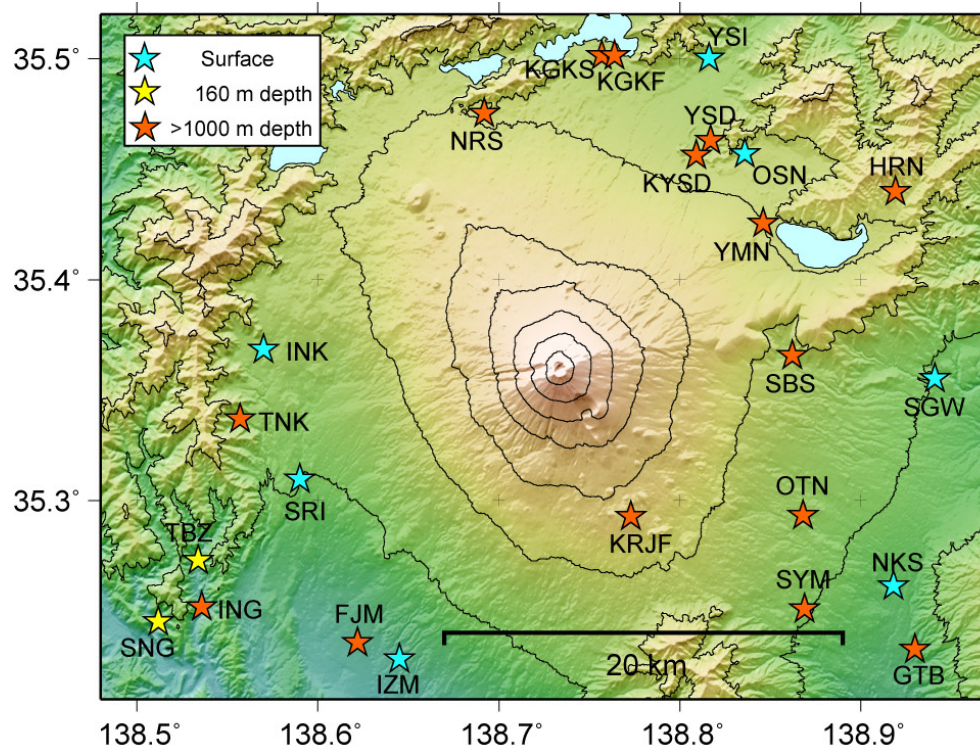


**Figure DR6.** Groundwater sampling sites surrounding Mt. Fuji, with their site names. All other notations are the same as in Figure 1.

Locality	Date (YYYY/MMDD)	Raw $^3\text{He}/^4\text{He}$ (Ra)	$^4\text{He}/^{20}\text{Ne}$	Corrected* $^3\text{He}/^4\text{He}$ (Ra)	$^4\text{He}$ ( $\text{cm}^3/\text{gH}_2\text{O}$ )	$^{20}\text{Ne}$ ( $\text{cm}^3/\text{gH}_2\text{O}$ )	Magmatic $^4\text{He}$ ( $\text{cm}^3/\text{gH}_2\text{O}$ )	Depth (m)
YSD-H	2010/2/19	5.92	2.72	6.43	5.17E-07	1.90E-07	4.15E-07	1500
YSD-C	2010/2/19	1.12	0.26	—	3.27E-08	1.26E-07	—	100
HRN	2010/2/20	0.96	0.30	—	3.73E-08	1.26E-07	—	1500
YMN	2010/2/19	3.86	0.87	5.06	1.44E-07	1.66E-07	9.11E-08	1500
NRS	2010/2/19	6.98	4.14	7.37	8.99E-07	2.17E-07	8.28E-07	1500
INK	2010/2/20	1.23	0.27	—	4.63E-08	1.72E-07	—	0
OSN	2010/2/19	1.22	0.25	—	4.09E-08	1.64E-07	—	0
SGW	2010/2/20	1.02	0.27	—	3.15E-08	1.16E-07	—	0
SBS	2010/3/24	5.06	1.08	6.31	1.67E-07	1.54E-07	1.32E-07	1500
NKS	2010/3/24	1.18	0.26	—	2.38E-08	9.15E-08	—	0
OTN	2010/3/24	3.98	3.16	4.24	6.88E-07	2.18E-07	3.65E-07	1500
YSI	2010/3/24	1.06	0.26	—	3.68E-08	1.39E-07	—	0
KYSD	2010/3/24	5.82	1.56	6.76	2.17E-07	1.39E-07	1.83E-07	1500
GTB	2010/3/24	4.57	0.65	—	7.08E-08	1.09E-07	—	1500
SYM	2010/3/25	6.48	114.51	6.49	3.71E-06	3.24E-08	3.01E-06	1300
I2M	2010/3/25	1.02	0.21	—	1.02E-08	4.95E-08	—	0
TBZ	2010/3/25	4.25	0.63	—	9.80E-08	1.55E-07	—	160
ING	2010/3/25	7.00	46.40	7.03	1.16E-05	2.50E-07	1.02E-05	1000
SNG	2010/3/25	5.47	15.13	5.54	1.80E-06	1.19E-07	1.25E-06	160
FJM	2010/3/26	7.65	23.09	7.72	4.71E-06	2.04E-07	4.55E-06	1500
SRI	2010/3/26	1.34	0.30	—	3.81E-08	1.27E-07	—	0
TNK	2010/3/26	1.26	5.71	1.28	1.37E-06	2.40E-07	2.19E-07	1300
KGKS	2010/3/26	7.35	18.49	7.44	2.20E-06	1.19E-07	2.05E-06	1500
KGSF	2010/3/26	7.33	87.50	7.35	1.05E-05	1.20E-07	9.64E-06	1500
KRJF	2012/2/21	7.44	6.72	7.69	2.01E-06	2.99E-07	1.93E-06	2000

**Table DR1.**  $^3\text{He}/^4\text{He}$  ratios from the groundwater sites surrounding Mt. Fuji. \*The  $^3\text{He}/^4\text{He}$  ratios have been corrected for air contamination by using  $^4\text{He}/^{20}\text{Ne}$  ratios. The locations of each sampling site are shown on Figure S6.

Locality	Date (YYYY/MMDD)	Resistivity ( $\Omega\text{m}$ )	Temperature ( $^{\circ}\text{C}$ )	Depth (m)	Na (mg)	K (mg)	Mg (mg)	Ca (mg)	Li (mg)	NH4 (mg)	Cl (mg)	SO4 (mg)	F (mg)	NO3 (mg)	NO2 (mg)	PO4 (mg)	Br (mg)	I (mg)	dD (‰)	d18O (‰)
YSD-H	2010/2/19	5.99	33.9	1500	119.1	1.9	0.0	317.6	0.00	0.0	49.5	894.5	0.1	0.0	0.0	0.0	0.1	0.0	-77.6	-11.16
YSD-C	2010/2/19	58.82	12.6	100	6.7	1.8	7.0	18.6	0.00	0.0	3.6	17.9	0.1	3.8	0.0	0.2	0.0	0.0	-64.6	-9.81
HRN	2010/2/20	64.94	17.6	1500	29.2	1.0	0.1	9.1	0.00	0.0	4.0	43.8	0.2	0.0	0.0	0.0	0.0	0.0	-62.9	-9.85
YMN	2010/2/19	47.62	25.6	1500	41.8	0.6	0.0	7.0	0.00	0.0	14.2	52.0	0.4	0.0	0.0	0.0	0.0	0.0	-78.1	-11.50
NRS	2010/2/19	6.29	31	1500	119.3	1.6	63.1	154.2	0.00	0.0	196.2	548.4	0.2	0.0	0.0	0.0	0.4	0.0	-85.1	-11.48
INK	2010/2/20	102.04	10.5	0	6.4	1.3	2.6	8.8	0.00	0.0	4.3	9.9	0.1	3.0	0.0	0.1	0.0	0.0	-61.1	-9.28
OSN	2010/2/19	61.73	11.5	0	6.6	1.8	6.8	17.8	0.00	0.0	3.3	7.9	0.1	7.8	0.0	0.4	0.0	0.0	-58.7	-8.89
SGW	2010/2/20	69.44	not measured	0	8.5	1.7	5.7	13.6	0.00	0.0	5.9	5.3	0.1	4.9	0.1	0.4	0.0	0.0	-52.5	-8.36
SBS	2010/3/24	28.57	36.9	1500	41.8	0.6	0.0	40.0	0.01	0.0	10.8	141.4	0.2	0.0	0.0	0.0	0.0	0.0	-65.5	-10.21
NKS	2010/3/24	63.69	14.7	0	19.4	2.2	5.2	13.5	0.01	0.0	18.4	7.5	0.1	3.9	0.0	0.3	0.1	0.0	-58.0	-9.20
OTN	2010/3/24	10.10	31.6	1500	155.9	13.1	2.8	46.1	0.01	0.0	143.2	204.7	0.3	0.0	0.0	0.0	0.4	0.0	-72.9	-11.03
YSI	2010/3/24	31.25	not measured	0	22.4	0.7	9.5	29.1	0.00	0.0	51.1	31.3	0.1	0.0	0.0	0.0	0.0	0.0	-64.8	-9.84
KYSD	2010/3/24	5.15	19.7	1500	152.7	3.3	0.1	358.3	0.00	0.0	85.3	1014.5	0.1	0.1	0.0	0.0	0.2	0.0	-84.9	-12.20
GTB	2010/3/24	32.26	42.3	1500	65.4	6.1	1.0	5.3	0.00	0.0	27.7	14.4	0.2	0.0	0.0	0.1	0.1	0.0	-50.6	-8.18
SYM	2010/3/25	0.63	40.8	1300	1711.8	87.5	33.9	1984.5	0.04	0.1	5879.8	231.9	0.4	0.4	0.0	0.0	16.5	0.0	-43.7	-7.51
I2M	2010/3/25	53.48	14.7	0	7.8	2.9	5.5	20.8	0.00	0.0	8.6	20.8	0.1	20.3	0.0	0.1	0.0	0.0	-50.8	-8.00
TBZ	2010/3/25	66.67	14.6	160	7.7	0.0	2.6	19.2	0.00	0.0	5.0	14.9	0.1	2.5	0.0	0.0	0.0	0.0	-50.6	-8.14
ING	2010/3/25	3.13	28.7	1000	279.1	0.6	0.1	382.7	0.01	0.3	1045.8	15.8	2.0	0.1	0.0	0.0	3.2	0.0	-46.8	-7.86
SNG	2010/3/25	10.31	30.1	160	147.1	0.6	0.0	47.4	0.03	0.6	274.0	21.5	0.6	0.0	0.0	0.0	0.7	0.1	-52.7	-8.33
FJM	2010/3/26	3.13	29.4	1500	425.2	11.1	44.1	288.6	0.00	0.0	671.9	709.4	0.1	0.0	0.0	0.3	1.5	0.0	-79.8	-11.58
SRI	2010/3/26	81.30	11.7	0	8.7	1.7	3.5	9.9	0.00	0.0	5.0	9.6	0.1	5.4	0.0	0.1	0.0	0.0	-58.0	-9.05
TNK	2010/3/26	28.57	22.3	1300	72.7	0.3	0.0	6.1	0.04	0.1	10.4	78.4	9.3	0.0	0.0	0.0	0.1	0.0	-67.1	-10.80
KGK-S	2010/3/26	5.00	24.2	1500	215.4	0.5	11.2	244.9	0.01	0.0	316.2	571.2	0.2	0.1	0.0	0.0	0.4	0.0	-77.9	-11.54
KGK-F	2010/3/26	3.45	33.4	1500	419.8	0.8	1.8	301.8	0.01	0.0	490.2	760.2	0.2	0.1	0.0	0.7	1.1	0.0	-71.5	-10.91
KRJF	2012/2/21	9.09	34.8	2000	490.3	9.0	35.2	183.0	0.00	0.0	224.8	1190.0	0.2	0.1	0.0	0.0	0.5	0.0	-78.1	-10.63

**Table DR2.** Chemical and isotopic compositions of groundwater surrounding Mt. Fuji. The electric resistivity values provided are at room temperature (15  $^{\circ}\text{C}$ ). The locations of each sampling site are shown in Figure S6.



	Depth	Date	d13C	DIC conc. (Total C)
Locality	(m)	(YYYY/MMDD)	(‰)	(mg/L)
YSD	1500	2013/11/29	-11.33	0.3
YMN	1500	2013/11/29	-14.65	2.4
NRS	1500	2013/11/28	-3.65	31.6
SBS	1500	2013/3/6	-10.87	1.3
OTN	1500	2013/3/6	-3.78	8.4
KYSD	1500	2013/11/29	-18.54	1.1
GTB	1500	2013/3/5	-5.76	22.8
SYM	1300	2012/3/29	-5.96	2.9
ING	1000	2012/3/26	-25.68	0.8
SNG	160	2012/7/24	-9.49	0.8
FJM	1500	2013/3/8	-9.88	12.6
TNK	1300	2015/7/2	-13.77	1.9
KMK	1500	2013/11/28	-10.35	0.4
KGKS	1500	2014/12/9	-1.64	46.3
KGSF	1500	2014/12/9	-4.11	31.6
NMB	1500	2012/7/2	-14.66	3.6
KRJF	2000	2015/7/2	-3.92	17.0

**Table DR3.**  $\delta^{13}\text{C}$  of DIC and the concentration of DIC of hot spring water surrounding Mt. Fuji. The locations of each sampling site are shown in Figure S6.